All-optical interrogation of millimeter-scale networks and application to developing ferret cortex

Haleigh N. Mulholland, Harishankar Jayakumar*, Deano M. Farinella*, Gordon B. Smith

Optical Imaging and Brain Sciences Medical Discovery Team, Department of Neuroscience, University of Minnesota, 2021 6th Street SE, Minneapolis, MN, 55455, USA

* Contributed equally

Correspondence to: Gordon Smith, gbsmith@umn.edu

Abstract

Background: Perception and behavior require coordinated activity of thousands of neurons operating in networks that span millimeters of brain area. *In vivo* calcium imaging approaches have proven exceptionally powerful for examining the structure of these networks at large scales, and optogenetics can allow for causal manipulations of large populations of neurons. However, realizing the full potential of these techniques requires the ability to simultaneously measure and manipulate distinct circuit elements on the scale of millimeters.

New method: We describe an opto-macroscope, an artifact-free, all-optical system capable of delivering patterned optogenetic stimulation with high spatial and temporal resolution across millimeters of brain while simultaneously imaging functional neural activity.

Results: We find that this approach provides direct manipulation of cortical regions ranging from hundreds of microns to several millimeters in area, allowing for the perturbation of individual brain areas or networks of functional domains. Using this system we find that spatially complex endogenous networks in the developing ferret visual cortex can be readily reactivated by precisely designed patterned optogenetic stimuli.

Comparison with existing methods: Our opto-macroscope extends current all-optical optogenetic approaches which operate on a cellular scale with multiphoton stimulation, and are poorly suited to investigate the millimeter-scale of many functional networks. It also builds upon other mesoscopic optogenetic techniques that lack simultaneous optical readouts of neural activity.

Conclusions: The large-scale all-optical capabilities of our system make it a powerful new tool for investigating the contribution of cortical domains and brain areas to the functional neural networks that underlie perception and behavior.

Keywords

Optogenetics, microscopy, calcium imaging, networks

1. Introduction

Sensory perception and behavior involve the coordinated activity of thousands of neurons arranged in functional networks that are spread across multiple brain regions, spanning millimeters of cortical area. For example, in the visual cortex, sensory stimuli evoke responses in populations of neurons whose activity is determined by the alignment of the stimulus to a broad range of tuning properties (Hubel and Wiesel, 1997). In species such as humans, other primates, and carnivores such as cats and ferrets, these selective neurons are organized into

locally clustered modular domains, with nearby neurons sharing selectivity for stimulus features such as retinotopic position, edge orientation, and ocular dominance (Blasdel and Salama, 1986; Hubel and Wiesel, 1968; Issa et al., 2000; Kara and Boyd, 2009; Smith et al., 2015; Weliky et al., 1996). Notably these populations can be distributed across the cortical surface, forming interconnected networks that span millimeters (Bosking et al., 1997; Gilbert and Wiesel, 1989; Malach et al., 1993). Similar large-scale organizational features exist in other cortical areas, including auditory and somatosensory cortex, where tonotopic and somatotopic representations exist (Kaas et al., 1979; Merzenich et al., 1975). Understanding the function of these large-scale networks is critical not only to determining the contribution of individual brain regions to complex behaviors, but also to uncovering how local perturbations impact global network function and give rise to neurological disorders.

Over the last decade, advances in optical imaging approaches have revolutionized the study of these functional networks. Optical approaches are often the optimal means for investigating these questions, combining the ability to collect data over a large area—thereby capturing the distributed nature of these networks—with the high spatial resolution needed to identify local precision. Hemodynamic approaches (Grinvald et al., 1986) and voltage sensitive dyes (Grinvald and Hildesheim, 2004) have largely been replaced with fast, highly sensitive genetically-encoded calcium indicators (Chen et al., 2013; Zhang et al., 2023), which provide high spatial resolution readouts of neural activity across large areas with high signal-to-noise-ratios and good temporal resolution. In addition to facilitating new insights into the organization of sensory cortices, these approaches have enabled the investigation of interactions between highly varied cortical regions. For example, simultaneously imaging the entire dorsal surface of the mouse cortex, researchers have revealed behaviorally-relevant functional networks that span many different cortical areas (reviewed in (Cardin et al., 2020; Ren and Komiyama, 2021)).

In parallel, the maturation of optogenetics has given researchers the ability to perform causal manipulations of network function. Since the development of the first optogenetic activators, genetic approaches have allowed the targeting of distinct cell types within networks (Deisseroth, 2015). However, the full potential of optogenetics is realized when these genetic tools are paired with the precise spatial and temporal control afforded by targeted optical stimulation, thereby allowing the targeted stimulation of single cells, local populations, or specific areas (Packer et al., 2013). Thus, by identifying functional networks through optical imaging and then specifically targeting identified network elements, investigators are able to probe the contribution of those specific elements to network function. Achieving this requires simultaneous imaging and stimulation, allowing both the identification of network elements and the ability to monitor the impacts of targeted optogenetic perturbations on network function. Current approaches to simultaneous imaging and optogenetic manipulation predominantly focus on manipulations at the single cell level, employing multiphoton stimulation and imaging (reviewed in (Adesnik and Abdeladim, 2021; Carrillo-Reid et al., 2017)). While extremely powerful, these techniques are restricted in both the number and spatial extent of neurons that can be manipulated, thus limiting their ability to investigate network organizations larger than several hundred microns.

In order to overcome these limitations and interrogate functional networks on a millimeter scale, we developed an opto-macroscope, an all-optical system capable of performing targeted optogenetic manipulations with high spatial and temporal resolution across millimeters of brain, while simultaneously measuring network activity via calcium imaging. Our system is designed to

allow simultaneous imaging without contamination of light artifacts from optogenetic stimulation, and can stimulate arbitrary regions ranging from hundreds of microns to several millimeters in area. Using our opto-macroscope, we find that both visually-driven and spontaneously occurring endogenous cortical networks in developing ferret visual cortex can be strongly re-activated by precisely patterned optogenetic stimulation. Our results demonstrate that our opto-macroscope allows functional modules identified via optical imaging to be specifically manipulated, permitting causal investigations of network function.

2. Materials and Methods

2.1 Microscope design

The key design goal of our opto-macroscope was to allow targeted optogenetic manipulations with high spatial and temporal precision while simultaneously imaging neural activity with high sensitivity. In this context, spatial precision refers to imaging and stimulation in a 2-dimensional plane across the brain surface. To achieve this, we designed our system to take advantage of the high sensitivity of GFP-based genetically encoded calcium sensors (e.g. GCaMP6 (Chen et al., 2013) or jGCaMP8 (Zhang et al., 2023)) in conjunction with red-shifted optogenetic tools, such as Chrimson (Klapoetke et al., 2014). With this approach, we sought to minimize the power of the blue-light excitation that is required for GCaMP imaging in order to avoid cross-talk with Chrimson, which has weak but non-zero photocurrents in response to the 470 nm excitation used for GCaMP (Klapoetke et al., 2014).

We designed our imaging system around a highly sensitive back-illuminated sCMOS camera with >90% quantum efficiency from 500-560 nm (Prime BSI Express, Teledyne Photometrics) (Figure 1a,b). Signal collection is further enhanced by using the available on-camera 2 x 2 binning, with images collected at 1024 x 1024 pixels. To optimize light collection, we utilize a tandem-lens macroscope (Ratzlaff and Grinvald, 1991) consisting of a 50 mm camera lens (Nikon AF NIKKOR F/1.4D) objective and a 105 mm camera lens (Nikon AF NIKKOR 105mm F/2D) as tube lens. The adjustable focus of each camera lens is set to infinity. The total magnification of the system is optimized for a ~4 mm diameter imaging FOV by increasing the magnification of the system to 3.4x with a f=-40 mm achromatic doublet (Thorlabs ACN254-040-A) placed prior to the camera, thereby filling the full area of the camera sensor with our target 4 mm FOV. GCaMP excitation is provided with a 470 nm LED (Thorlabs M470L4) coupled to a condenser lens (Thorlabs ACL252OU-DG6-A) and a 469 nm bandpass filter (Thorlabs MF469-35). A 495 nm dichroic mirror (Chroma T495lpxr) is used to separate excitation and GCaMP emission, which is collected through a 525 nm bandpass filter (Edmund Optics 86-984). Filter wavelengths and bandwidths were chosen to maximize GCaMP collection while eliminating contamination with optogenetic stimulation light (see below) (Figure 1c). Spectra shown in Figure 1c were obtained from various sources: optical elements from manufacturer information, GCaMP6s from (Chen et al., 2013), and stimulation laser from direct spectrophotometer measurement.

Optogenetic stimulation is provided by a vertically polarized, 1 Watt 590 nm CW laser (Coherent MX590-1000 STM OPSLaser-Diode). Stimulation light is up-collimated by 2X and its polarization is rotated 90° before entering a power control acousto-optical modulator (AOM, Quanta-tech MTS110-A3-VIS). The zero-order beam is directed to a beam dump with a knife-edge right angle prism, and the first-order diffracted beam is then coupled into a 0.22NA 400µm multi-mode fiber on the input of a speckle remover (Changchun New Industries) which is

subsequently delivered to the input of a DMD module (Mightex POLYGON1000-DL). The optics comprising the stimulation arm relay were chosen such that the stimulation field slightly overfills the imaging area while maintaining sufficient power density for opto-genetic stimulation. Stimulation light is directed through a tube lens (f=100 mm, Mightex) and is filtered by a band-pass filter (Chroma et590/33m) and reflected toward the sample by a short-pass dichroic beamsplitter (Thorlabs DMSP567L). Following reflection, stimulation light is transmitted through the 495 nm long-pass dichroic beamsplitter in the imaging arm before arriving at the objective back aperture. The stimulation tube lens and the 50 mm objective lens form an image relay conjugating the surface of the DMD chip to the image plane providing a stimulation field of ~ 4.1 mm. To eliminate light artifacts and prevent stimulation light from reaching the sCMOS camera, a 561 nm short pass filter and 594 nm notch filter are installed in the light path prior to the camera.

To ensure that the imaging and stimulation paths are parfocal, a low intensity grid pattern generated by the DMD was projected onto the surface of a mirror located in the sample plane through the stimulation arm of the opto-macroscope. Slight adjustments in mirror position along the optical axis were made with camera feedback to ensure the mirror was located precisely in the DMD conjugate plane (where the grid is sharply reconstructed). The image of this grid pattern was then relayed through the imaging path to the sCMOS camera with the bandpass, shortpass and notch filters removed to allow some laser light to reach the camera. Parfocality was achieved by fine-tuning the separation between the 105 mm tube lens, the -40 mm achromatic doublet, and the camera.

Stimulation timing and power are controlled through a custom-written Python-based computer interface. Power control waveforms are sent to the analog input of the AOM driver through a DAQ board (Measurement Computing USB-1208FS). The custom software includes a power calibration module, where the power under the opto-macroscope objective is recorded while sweeping the input voltage to the AOM driver. Acquired data is fit with the complementary error function in scipy (Virtanen et al., 2020), and used to convert specified output power to command voltages that are input to the AOM. In order to precisely record stimulation timing, we took advantage of the small amount of stimulation light that leaks through the 567 nm short-pass dichroic in the stimulation arm. This light is relayed onto the surface of a large area photodiode (Thorlabs SM05PD1A) using a compound lens (Thorlabs AC508-100-A, and Thorlabs LB1811, f = 26 mm). Back-reflections from this path are minimized by installing the photodiode at an angle to the optical path. To further mitigate back-reflections originating from the photodiode, yet still allow for sufficient power for detection at the photodiode, an angled OD 1 filter (Thorlabs NE2R10A) is installed prior to the photodiode. Spatial stimulation patterns are generated through Mightex Polyscan2 software, which transforms stimulation patterns to the imaging frame of reference, allowing direct targeting of specified regions of the image. For fast switching between stimulation patterns, target stimulation patterns or blank (no stimulation) patterns are pre-loaded onto the Polygon, which is then operated in ‘follower’ mode. Pattern switching is then triggered externally from the DAQ board in conjunction with any desired modulations in laser power.

2.2 Quantification of optical properties

The spatial resolution of the imaging pathway was assessed with a 1951 USAF test target slide (Thorlabs) which has a maximum resolution of 228.0 lp/mm. To assess the fidelity of

stimulation patterns and the stimulation resolution, we projected arbitrary patterns (including checkerboards and 1951 USAF test patterns) on an autofluorescent plastic slide (Chroma) placed at the sample plane, which has a broad emission spectrum that allows the fluoresced stimulation pattern to reach the camera. The resolution of single stimulation pixels was measured by projecting a grid stimulus with 1 pixel thick lines. The projected pattern was directly recorded with a camera (Mightex SME-B012-U) placed at the sample plane. The horizontal and vertical lateral resolution was measured in 100 μm segments across grid lines. Segments were averaged and fitted with a Gaussian function, from which the stimulation resolution was calculated.

The axial resolution of the imaging pathway was measured by translating a sample of well-isolated 15 μm beads (ThermoFisher FocalCheck F7239) around the focal plane in 5 μm steps. The axial resolution of the stimulation pathway was quantified by projecting a 40 x 40 μm stimulus onto a camera placed at the focal plane, which was then translated in 5 μm steps. X-Z projection images were then measured and fitted with a Gaussian function.

The spatial uniformity of stimulation light was quantified by projecting 125 x 125 μm squares in a grid pattern covering the FOV while recording power with a power meter (Thorlabs) placed at the sample plane. Spatial uniformity was also assessed by projecting a full-area stimulation onto a camera (Mightex) placed at the sample plane after attenuating the stimulation light with an OD3 neutral density filter (Thorlabs). Contrast ratio for both uniformity datasets was then calculated as:

$$Contrast\ ratio = \frac{\max(P) - \min(P)}{\max(P) + \min(P)}$$

where P is the power (counts) measured for each stimulation square (pixel), within the 3.8 mm addressable area. The coefficient of variation across the stimulation FOV was calculated as:

$$CV = \frac{\sigma_P}{P}$$

The stability of the excitation 470 nm LED for GCaMP imaging was assessed by illuminating a static sample comprised of a dilute fluorescein bath with the same excitation power used for all *in vivo* imaging experiments. Emitted fluorescence was collected through the imaging pathway and analyzed as with GCaMP data (see below). In addition, stability of both the 470 nm LED and 590 nm stimulation illumination was measured by directly placing a power meter at the sample plane.

To quantify the temporal capabilities of the opto-macroscope, we constructed arbitrary power waveforms consisting of both upwards and downwards power ramps and sweeps of pulse duration from 1 second to 1 ms. Timing was assessed by placing a fast photodiode (Thorlabs DET50B2) at the sample plane while projecting a full-field pattern of stimulation.

2.3 Animals

All experimental procedures were approved by the University of Minnesota Institutional Animal Care and Use Committee and were performed in accordance with guidelines from the US National Institutes of Health. We obtained male and female ferret kits from Marshall Farms and housed them with jills on a 16 h light/8 h dark cycle.

2.4 Viral injection

Viral injections and cranial window implants were performed as previously described (Smith et al., 2018; Smith and Fitzpatrick, 2016). Briefly, we microinjected a 1:1 ratio by volume of AAV1.hSyn.GCaMP6s.WPRE.SV40 (Addgene, $2.5*10^{13}$ GC/ml) and the somatically targeted AAV1.hSyn.ChrimsonR.mRuby2.ST (University of Minnesota Viral Vector and Cloning Core, $1.32*10^{13}$ GC/ml) into layer 2/3 of the primary visual cortex at P10–15, approximately 10–15 days before imaging experiments. In experiments testing potential artifacts from optogenetic stimulation light, ChrimsonR was omitted, and only AAV expressing GCaMP6s was injected. Anesthesia was induced with isoflurane (3.5–4%) and maintained with isoflurane (1–1.5%). Buprenorphine (0.01 mg/kg) and glycopyrrolate (0.01 mg/kg) were administered, as well as 1:1 lidocaine/bupivacaine at the site of incision. Animal temperature was maintained at approximately 37°C with a water pump heat therapy pad (Adroit Medical HTP-1500, Parkland Scientific). Animals were mechanically ventilated and both heart rate and end-tidal CO2 were monitored throughout the surgery. Using aseptic surgical technique, skin and muscle overlying visual cortex were retracted. To maximize area of ChrimsonR expression, two small burr holes placed 1.5-2 mm apart were made with a handheld drill (Fordom Electric Co.). Approximately 1 µl of virus contained in a pulled-glass pipette was pressure injected into the cortex at two depths (~200 µm and 400 µm below the surface) at each of the craniotomy sites over 20 min using a Nanoject-III (World Precision Instruments). The craniotomies were filled with 2% agarose and sealed with a thin sterile plastic film to prevent dural adhesion, before suturing the muscle and skin.

2.5 Cranial window surgery

On the day of experimental imaging, ferrets were anesthetized with 3–4% isoflurane. Atropine (0.2 mg/kg) was injected subcutaneously. Animals were placed on a feedback-controlled heating pad to maintain an internal temperature of 37–38°C. Animals were intubated and ventilated, and isoflurane was delivered between 1% and 2% throughout the surgical procedure to maintain a surgical plane of anesthesia. An intraparietal catheter was placed to deliver fluids. EKG, end-tidal CO2, and internal temperature were continuously monitored during the procedure and subsequent imaging session. The scalp was retracted and a custom titanium headplate adhered to the skull using C&B Metabond (Parkell). A 6–7 mm craniotomy was performed at the viral injection site and the dura retracted to reveal the cortex. One 4 mm cover glass (round, #1.5 thickness, Electron Microscopy Sciences) was adhered to the bottom of a custom titanium insert and placed onto the brain to gently compress the underlying cortex and dampen biological motion during imaging. The cranial window was hermetically sealed using a stainless-steel retaining ring (5/16-in internal retaining ring, McMaster-Carr). Upon completion of the surgical procedure, isoflurane was gradually reduced (0.6–0.9%) and then vecuronium bromide (0.4 mg/kg/hr) mixed in an LRS 5% dextrose solution was delivered IP to reduce motion and prevent spontaneous respiration.

2.6 In vivo widefield epifluorescence imaging and optogenetic stimulation

Widefield epifluorescence imaging was performed with µManager software (Edelstein et al., 2010). Images were acquired from the opto-macroscope at 15 Hz with 2 × 2 on camera binning and additional offline 2×2 binning to yield 512 × 512 pixels. In order to measure the structure of endogenous networks in the visual cortex, we recorded visually-evoked responses to full-field luminance changes as well as ongoing spontaneous activity in the absence of visual stimulation.

Visual stimuli were delivered on an LCD screen placed approximately 22 cm in front of the eyes. Through closed eyelids, full-field change-in-luminance stimuli were used to evoke ON and OFF responses, with a Michelson contrast of 1. Stimuli were presented using Psychopy software (Peirce, 2007) for 5 seconds ON, 5 seconds OFF. Image series were motion corrected using rigid alignment and a region of interest (ROI) was manually drawn around the cortical region of GCaMP expression. The baseline fluorescence (F_0) for each pixel was obtained by applying a rank-order filter to the raw fluorescence trace with a rank 70 samples and a time window of 30 s (451 samples). The rank and time window were chosen such that the baseline faithfully followed the slow trend of the fluorescence activity. The baseline-corrected spontaneous activity was calculated as: $\Delta F/F_0 = (F-F_0)/F_0$. Individual ON or OFF evoked-events were obtained by averaging evoked responses over the first 2 seconds following stimulus onset, and ON/OFF maps were calculated by taking the average ON or OFF response across trials, with difference maps showing the difference between ON – OFF responses.

Spontaneous activity was captured over a 10-min imaging session, with the animal sitting in a darkened room facing an LCD monitor displaying a black screen. Images were motion corrected and $\Delta F/F_0$ calculated as above. Spontaneous events and correlation patterns were detected as described (Smith et al., 2018). Briefly, active pixels on each frame were identified with a threshold set at 5 s.d. above the mean across time, and spontaneous events were taken as frames with a spatially extended pattern of activity (>80% of pixels within the ROI were active). Events were spatially filtered (σ_{low}=26 μm and σ_{high}=195 μm), and downsampled to 128 x 128 pixels). Spontaneous networks were identified by taking the pairwise Pearson's correlation between all pixels in the ROI, using the single maximally active frame from each event.

Single spot optogenetic stimulation ROIs were created by arbitrarily targeting four non-overlapping 390 μm diameter circles across the FOV. Endogenously–derived optogenetic stimulation patterns were based on online analysis of naturally occurring patterns (either OFF-preference domains, or correlated regions in spontaneous activity). Stimulation masks were generated by manually drawing ROIs around targeted domains. For both single spot and endogenously-derived patterns, stimuli were then delivered for 1 second. Optical stimulation power was delivered at 7.6 mW/mm^2 , though significant increases in calcium fluorescence could be detected at powers greater than or equal to 1 mW/mm^2 , consistent with the threshold to spike probability for Chrimson (Klapoetke et al., 2014). At the powers used here (7.6 mW/mm^2 Chrimson stimulation, <=0.06 mW/mm^2 GCaMP excitation), we saw little evidence of photobleaching of either the GCaMP sensor or the Chrimson opsin, and opto-evoked activity remained robust across repeated, intermittent optogenetic stimulation trials over the course of the experiment day (the longest period being 12 hours). Optogenetic stimulation was delivered in the absence of visual input, and the animal's eyes were shielded from the stimulation laser to prevent indirect stimulation of the retina. To better visualize responses evoked by spatially patterned stimuli, spatially filtered responses (right image in Figure 5f,l) were obtained using a Gaussian spatial band-pass filter (σ_{low}=26 μm and σ_{high}=195 μm).

To test for light artifacts in fluorescent, biological tissue, we optogenetically stimulated *in vivo* ferret V1 in an animal expressing GCaMP6s but not Chrimson. Isoflurane was increased to 2% to limit ongoing spontaneous activity. Using a uniform, full field-of-view optogenetic stimulus, we incrementally increased the power to a maximum of 10.6 mW/mm^2 (n trials=10). Normalized fluorescence counts (ΔF) of the average activity across the field of view were calculated by

subtracting the baseline fluorescence (F_0). F_0 across the field of view was obtained by applying a median filter to the raw fluorescence trace within a time window of 2 s (60 samples). To compare these counts to functional data, this same signal extraction approach was used on a spontaneous activity trial from the same animal (isoflurane 0.6-0.9%).

2.7 Histology and confocal imaging

For a subset of animals, following imaging animals were euthanized and transcardially perfused with 0.9% heparinized saline and 4% paraformaldehyde. The brains were extracted, post-fixed overnight in 4% paraformaldehyde, and stored in 0.1 M phosphate buffer solution. Brains were cut using a vibratome in 50 µm coronal sections, which were then imaged on a confocal microscope (Nikon AX R).

3. Results

3.1 Optical characteristics of opto-macroscope for imaging and stimulation

To assess the optical characteristics of the opto-macroscope, we first tested its ability to effectively produce desired spatial stimulation patterns at the sample plane. When tested with a variety of patterns, including single or multiple spots, or more complex patterns such as a checkerboard, the input stimulus pattern was in all cases accurately relayed to the sample plane (Figure 2a). We next quantified the field-of-view (FOV) and spatial resolution of both the imaging and stimulation pathways using 1951 USAF resolution targets. The imaging FOV was 3.87 x 3.87 mm, with a spatial resolution of 3.78 µm/px, and target elements up to 143.7 lp/mm were resolvable (Figure 2b). To assess the resolution of the stimulation pathway, we used these same test targets as the input to the DMD stimulator, and imaged the pattern produced at the sample plane. These tests show that the addressable area is approximately a 3.8 mm diameter circle centered in the imaging FOV, with the corners of the imaging FOV not reachable with stimulation light (Figure 2a,c). Within this addressable FOV, stimulation resolution assessed with USAF target stimulation was greater than 40.3 lp/mm, corresponding to a line width of 12.4 µm. To determine the smallest features that could be addressed with our stimulation pathway, we projected an input consisting of a single-pixel wide grid, measuring a resolution of 8.0 µm full-width at half-max (FWHM) and 14.8 µm full-width at tenth-max (FWTM) in both X and Y (Figure 2d), in agreement with our results from the USAF test target.

In order to assess the axial resolution of our system, we first imaged well-isolated 15 µm beads with our imaging path. As expected from an epi-fluorescence microscope, the point-spread function was elongated axially, with a FWHM of 151 µm, while maintaining good lateral resolution (Figure 2e, *left,* Figure 2f, *top*, lateral FWHM: 11.8 µm, FWTM: 21.6 µm). Stimulation with a 40 x 40 µm square produced a highly elongated axial pattern, with an axial FWHM of 594 µm (Figure 2e, *right*). Notably, despite this pronounced axial elongation, the lateral resolution was maintained, with lateral FWHM less than 60 µm within ±200 µm of the focal plane (Figure 2f, *bottom*).

Finally, we measured the uniformity of stimulation power across our addressable FOV, using two complementary approaches. First, in order to provide a direct readout of stimulation power, we placed a highly sensitive photodiode-based power meter (Thorlabs S170C) at the sample plane while stimulating with 125 µm squares in a 30 x 30 grid. We found that the intensity of stimulation light was relatively uniform (Figure 2g), with a contrast ratio of 0.25, and

a coefficient of variation of 0.09. Importantly, the available power density at all locations within the 3.8 mm addressable FOV exceeds 10 mW/mm^2, well above the 1 mW/mm^2 required to elicit spikes with Chrimson (Klapoetke et al., 2014). As the minimum size of our grid stimulation squares was limited by the sensitivity of our power meter, we also measured the uniformity of stimulation by projecting an attenuated full-field stimulus directly onto a camera sensor placed at the sample plane, providing 3.75 μm resolution of the stimulation uniformity (Figure 2h). These results agreed well with our power meter-based measurements, with a contrast ratio of 0.26, and a coefficient of variation of 0.07. Thus, the opto-macroscope is capable of both imaging and stimulating at high spatial resolution over a large 2-dimensional area.

A key design requirement of our microscope is the ability to image neural activity while simultaneously delivering optogenetic stimulation. Thus, it is essential that any light artifacts from optogenetic stimulation be minimal compared to fluorescence collected through the imaging path. Our design sought to achieve this both through optimized light collection to maximize the amount of GCaMP emitted signal that we collect, and through filter selection to prevent contamination from 590 nm stimulation light. We tested the efficiency of GCaMP signal collection by imaging an *in vivo* ferret brain expressing only GCaMP6s (without Chrimson), finding that high SNR images consistent with prior work (Mulholland et al., 2021; Smith et al., 2018, 2015) could be obtained with low 470 nm excitation power (<=0.06 mW/mm^2), below the threshold for activating Chrimson with blue light (Klapoetke et al., 2014). We next delivered full-area 590 nm stimulation at increasing power levels and measured the resulting change in fluorescence counts on the camera. We observed that stimulation artifacts were undetectable even at the highest stimulation powers and were in all cases several orders of magnitude smaller than the changes in GCaMP fluorescence resulting from neural activity (Figure 2i, black, green lines). Notably these changes in GCaMP fluorescence were themselves much larger than fluctuations in excitation intensity, which we assessed by imaging a static bath of dilute fluorescein (Figure 2i, blue line). The stability of GCaMP excitation intensity was further supported by direct measurements of excitation power, which also showed very low fluctuations over time (coefficient of variation (CV) = 6.5 x 10^{-4} over 25 seconds, 2.0 x 10^{-4} over 40 minutes).

Lastly, we assessed the stability stimulation power in the opto-macroscope through repeated measurements from a power meter placed at the sample plane. Stimulation power was highly stable on the timescale of both seconds (Figure 2j, *bottom*, CV = 0.6 x 10^{-3}, 25 sec) and minutes (Figure 2j, *top*, CV = 1.1 x 10^{-3}, 40 min).

3.2 Fast temporal control of stimulation patterns

A principal feature of our system is the ability to rapidly modulate stimulation power with an AOM, allowing for complex and arbitrary waveforms. This is key for many optogenetic experiments, as ramping stimuli (both increasing and decreasing stimulation intensity) are commonly used to induce specific network behavior (e.g. (Adesnik and Scanziani, 2010; Akam et al., 2012)) or avoid offset rebound artifacts (e.g. (Chuong et al., 2014)). To test our ability to deliver complex temporally precise power control for optogenetic stimuli, we delivered full-area stimuli while modulating stimulus power with an arbitrary waveform consisting of either linear upwards and downwards ramps or square pulses of varying duration and frequency, while measuring the resulting output. Ramp stimuli faithfully produced linear ramps in output power (Figure 3a), and we were able to accurately deliver complex waveforms of increasing pulse

frequency that swept pulse durations over an order of magnitude from 1 second to 1 ms (Figure 3b,c).

To test the ability to produce complex spatial and temporal stimulus patterns, we interleaved two distinct spatial stimulus patterns (Figure 3d), initially with equivalent power for both stimuli. Measuring stimulation intensity in distinct regions of our FOV corresponding to each stimulus pattern shows the combined specificity in both spatial (2-D) and temporal dimensions (Figure 3e). We next utilized our fast power control to deliver differing laser power independently to each stimulus, which we observed was accurately reflected at the sample plane (Figure 3f). Thus, our opto-macroscope is capable of delivering complex optogenetic stimulation with high degrees of both spatial and temporal specificity.

3.3 Local stimulation of cortical domains *in vivo*

We next sought to test the ability of our opto-macroscope to produce spatially-specific optogenetic activation of neural activity over large areas *in vivo*. For our studies, we utilized a somatically-targeted (ST) version of ChrimsonR (Baker et al., 2016) in order to increase the spatial specificity of stimulation by reducing activation of neurons at non-targeted locations via activation of their dendrites. In developing ferrets (postnatal day 25-31) expressing both GCaMP6s and ChrimsonR-ST in excitatory neurons in visual cortex, we observed robust expression of both constructs in both layer 2/3 and in layer 5, with reduced expression in L4, as has been observed previously with AAV-expressed GCaMP in ferrets (Smith et al., 2018) (Figure 4a-c).

To drive activity, we delivered a series of local stimuli (390 μm diameter circles) targeted to distinct, arbitrarily chosen local areas within our imaging window (Figure 4d). For all stimulus locations, optogenetic activation resulted in a spatially-localized region of activation that was readily detectable as a location-specific increase in GCaMP signal (Figure 4e). Within the stimulated regions, responses were reliably evoked across multiple trials (Figure 4f). We observed that evoked responses were largely specific to the stimulated region, although we occasionally observed activation in other areas, likely through synaptic transmission and network activity within the brain. We quantified the spatial extent of activation and observed that evoked responses fell-off rapidly outside the stimulated ROI (Figure 4g).

In order to determine the smallest stimulus that could reliably evoke a response, we stimulated with circular stimuli of increasing diameter. Very small stimuli of 0.17 mm diameter or smaller failed to evoke consistent responses, whereas responses were reliably evoked for stimuli 0.32 mm and larger (Figure 4h). Notably, this diameter is roughly equivalent to the 300-400 μm size of cortical columns in the ferret (Kaschube et al., 2010), suggesting that it in part reflects endogenous network properties. We also observed that the degree of activation increased as stimulus size increased, presumably as a result of increased recruitment of neurons within the cortical network. Notably, when we repeated this experiment in animals lacking Chrimson and expressing GCaMP only, we failed to observe any activation in response to stimulation (Figure 4h, gray line), demonstrating specific optogenetic activation with Chrimson and ruling out non-specific effects such as stimulation light entering the animal's eyes.

3.4 In vivo stimulation with complex endogenous spatial patterns

One of the key advantages of our system relative to previous optogenetic approaches is the ability to stimulate large-scale, spatially complex patterns while simultaneously imaging neural

activity, allowing for the stimulation of biologically relevant functional networks. Such an approach would allow for causal investigation of the input-output transform of endogenous networks, such as the emergence of visually evoked and spontaneous activity that occurs during development (Chapman et al., 1996; Smith et al., 2018). We used this capability to investigate whether endogenous networks in the developing ferret visual cortex could be readily re-activated by artificial patterned optogenetic input applied directly to the cortex. Ferret visual cortex is known to contain spatially distributed functional networks reflecting a columnar encoding of visual features (Chapman et al., 1996).

We first examined whether the columnar representation of luminance step polarity (the selectivity for luminance increments – ON – versus luminance decrements – OFF) (Smith et al., 2015) could be driven by direct cortical activation. To determine the spatial layout of ON and OFF domains in the cortex, we first presented visual stimuli consisting of full-field luminance steps. While the response to increases in luminance (ON) was weak, luminance decrements (OFF) evoked responses that were strong and highly modular, in accordance with prior results (Figure 5a,b). We then used these OFF domains to design a patterned optogenetic stimulus (Figure 5c) that was then projected onto the cortex. Stimulation with this complex and endogenously-derived spatial pattern evoked strong and spatially organized responses that displayed a high level of similarity to the OFF functional network (Figure 5d-f). While these stimulated domains showed strong activation well-aligned to the OFF domains, we also observed a weak global activation across much of our imaging FOV, in contrast to the more specific results seen with single ROI stimuli (Figure 4). This could reflect a general increase in overall activity within the cortical network due to simultaneously driving multiple domains across the imaging area, as well as non-specific GCaMP signal from neuropil extending outside stimulated regions. Nonetheless, the spatial pattern corresponding to the targeted OFF-domains was readily apparent and superimposed on this more global activation, thereby demonstrating our ability to selectively re-activate a visually-driven network through patterned optogenetic stimulation.

In addition to being evoked through visual stimulation, functional networks in the visual cortex are also readily apparent in the patterns of ongoing spontaneous activity (Kenet et al., 2003), and spatial correlations in spontaneous activity have been used to identify such networks during early development (Mulholland et al., 2021; Smith et al., 2018). We therefore sought to determine if such spontaneously active endogenous networks could likewise be selectively activated through patterned optogenetic stimulation. We imaged ongoing spontaneous activity and computed spatial correlations across spontaneous events to identify correlated network domains (Figure 5g,h). As seen previously (Mulholland et al., 2021; Smith et al., 2018), correlation patterns varied for different seed points across the cortical surface, revealing the presence of multiple correlated networks within the visual cortex. We then selected one such correlated network for optogenetic stimulation, designing a stimulation pattern based on positively correlated regions for a single seed point (Figure 5i). When stimulating with this pattern, we observed patterned evoked responses that corresponded strongly with the structure of correlated spontaneous activity (Figure 5j-l), demonstrating the successful re-activation of this endogenous functional network. Together, these results show that distributed functional networks in the cortex, both reflecting selectivity for visual features or correlated spontaneous activity, can be selectively activated and manipulated through patterned stimulation using our opto-macroscope.

4. Discussion

Neural networks operate across a range of spatial scales. Fine-scale structure at cellular resolution can be examined with approaches that utilize two-photon imaging and holographic optogenetics. Here we sought to develop an approach to investigate functional networks at a larger scale. Our opto-macroscope is designed to probe neural networks by allowing simultaneous optical imaging and optogenetic manipulation over millimeters of brain area with high spatial and temporal precision. By combining the power of widefield optical imaging to assay network function with the ability to directly and flexibly manipulate those networks, our opto-macroscope opens the door to investigate a wide range of network phenomena.

The opto-macroscope described here extends prior designs (Roy et al., 2016; Wilson et al., 2018)—which allowed optogenetic stimulation over similar millimeter spatial scales—by adding the ability to simultaneously image neural activity with highly-sensitive calcium indicators. Those prior designs utilized modified DMD-based overhead projectors to provide patterned optogenetic stimulation, whereas the laser input in our system provides several key advantages. First, it provides stimulation light over a narrow spectral bandwidth, meaning that higher intensity stimulation is possible while reducing the total light reaching the cortex, thus avoiding unnecessary heating and photodamage. Secondly, it allowed us to implement AOM-based power modulation, allowing for the implementation of fast arbitrary stimulus waveforms. In addition, by basing our opto-macroscope around 590 nm optogenetic stimulation, our system is readily adaptable to other red-shifted optogenetic probes. Critically, this includes halorhodopsin, which can be readily activated with the same stimulation wavelength (Gradinaru et al., 2010), allowing for spatially targeted optogenetic inhibition of specific elements of functional neural networks.

There are several limitations of our opto-macroscope that restrict its use in certain applications. By designing around a green reporter (GCaMP) and red-shifted activator (Chrimson), we maximized the combination of imaging SNR and optogenetic photocurrent. However, Chrimson, like all currently known red-shifted channelrhodopsins, can be weakly activated by the blue light used to excite GCaMP (Klapoetke et al., 2014), and therefore care must be taken to keep excitation intensities as low as possible. Our opto-macroscope achieves this by utilizing a highly sensitive sCMOS camera, allowing us to use low excitation power and still achieve high GCaMP SNR. An additional limitation arises from the design decision to target stimulation over an approximately 3.8 mm diameter FOV, leading to a stimulation resolution of approximately 20 μm. Thus, the opto-macroscope is optimal for addressing targets on the scale of hundreds of microns or larger. However, relatively straightforward changes in the objective lens (e.g. to a 35 mm or 105 mm lens) can allow other labs to adjust the balance of area and spatial resolution to their experimental needs. Finally, though we demonstrate we can image and stimulate with high spatial resolution along the lateral axis, as with all single-photon optics our opto-macroscope is less spatially precise along the axial axis. While this broad axial spread may be useful when targeting functionally-linked columnar elements, it does not offer the axial precision of 2-photon optogenetic approaches.

Our opto-macroscope is designed to investigate functional relationships on a mesoscopic or columnar scale. The developing ferret visual cortex exhibits such a columnar or modular functional organization, with correlated domains on the scale of several hundred microns that are organized into correlated networks that extend over millimeters (Mulholland et al., 2021;

Smith et al., 2018), making it an ideal application for our opto-macroscope. Our results reveal that arbitrary cortical domains as well as millimeter scale functional networks can be reliably and selectively engaged with patterned input, while also raising several intriguing questions for future study. Stimulation with individual ROIs on the scale of functional modules (Figure 4) showed a degree of variability across ROIs both in terms of response amplitude within the ROI and in the ability to recruit additional active domains outside the stimulated area (e.g. ROI 3 in Figure 4e). It is possible that these differences are related to the underlying structure of the endogenous cortical network, with some ROIs perhaps better aligned to this structure and thereby better able to recruit additional network elements. Fully investigating this relationship will require further experiments, for example by using the opto-macroscope to systematically vary the stimulus location of columnar sized ROIs across the cortex and relating the resulting activation patterns to endogenous networks measured through spontaneous activity.

Our finding that millimeter-scale endogenous networks could be reliably driven with patterned input (Figure 5) provides an opportunity to investigate the extent to which the activity of cortical neurons is driven by the structure of feed-forward inputs as opposed to being shaped by intracortical networks. Addressing this question has been challenging, as it is often difficult to directly manipulate the structure of inputs to the cortex. Our opto-macroscope overcomes these limitations, allowing future studies to drive the cortex with both endogenous activity patterns as well as arbitrary structured patterns, in order to determine the degree to which cortical activation is governed by the similarity of an input to endogenous network structure.

We demonstrated our opto-macroscope in ferret visual cortex, where response properties and the corresponding neural networks are organized into columnar maps that are distributed across the cortical surface (Blasdel and Salama, 1986; Hubel and Wiesel, 1968; Issa et al., 2000; Kara and Boyd, 2009; Kenet et al., 2003; Smith et al., 2018, 2015; Weliky et al., 1996). However the utility of the opto-macroscope is not likely to be limited to this preparation. With the continued success in implementing optogenetic approaches to other species with columnar cortices such as the macaque (Tremblay et al., 2020), our opto-macroscope is well-suited to investigating causal relationships within large-scale networks and their role in behavior. Additionally, several recent publications have described large transparent cranial windows allowing optical access to the full dorsal cortex in mice and rats (eg (Ghanbari et al., 2019; Musall et al., 2019)). Widefield imaging using this approach has revealed functional networks that span multiple brain regions across millimeters that appear to underlie complex behaviors such as self-initiated locomotion (West et al., 2022). Our opto-macroscope would allow optogenetic manipulations to test functional relationships within these networks and their role behavior. Thus, by providing a flexible platform for targeted optogenetic interrogation of functional neural networks at millimeter-scale, our opto-macroscope enables a broad range of studies to uncover causal relationships in the brain.

Author contributions

Author contributions:

Conceptualization: HNM, GBS

Methodology: HNM, HJ, DMF, GBS

Investigation: HNM, HJ, DMF

Formal Analysis: HNM, DMF

Visualization: HNM, DMF

Funding acquisition: GBS

Project administration: GBS

Supervision: GBS

Writing – original draft: GBS

Writing – review & editing: HNM, HJ, DMF, GBS

Acknowledgements

We would like to thank Jack Kapler, and Sophie Bowman for experimental support, and members of the Smith lab for helpful discussions. This research was supported by National Eye Institute (NIH R01EY030893-01) (GBS), Whitehall Foundation (2018-05-57) (GBS), and National Science Foundation (IIS-2011542) (GBS). This work was supported by the resources and staff at the University of Minnesota University Imaging Centers (RRID: SCR_020997). Viral vectors used in this study were generated by the University of Minnesota Viral Vector and Cloning Core (Minneapolis, MN).

Materials availability

A full parts list is available from the corresponding author upon request. All custom code for calibration of AOM power output is available upon request.

Competing interests

The authors declare no competing financial interests.

References

Adesnik, H., Abdeladim, L., 2021. Probing neural codes with two-photon holographic optogenetics. Nat. Neurosci. 24, 1356–1366. https://doi.org/10.1038/s41593-021-00902-9

Adesnik, H., Scanziani, M., 2010. Lateral competition for cortical space by layer-specific horizontal circuits. Nature 464, 1155–1160. https://doi.org/10.1038/nature08935

Akam, T., Oren, I., Mantoan, L., Ferenczi, E., Kullmann, D.M., 2012. Oscillatory dynamics in the hippocampus support dentate gyrus–CA3 coupling. Nat. Neurosci. 15, 763–768. https://doi.org/10.1038/nn.3081

Baker, C.A., Elyada, Y.M., Parra, A., Bolton, M.M., 2016. Cellular resolution circuit mapping with temporal-focused excitation of soma-targeted channelrhodopsin. Elife 5, e14193. https://doi.org/10.7554/eLife.14193

Blasdel, G.G., Salama, G., 1986. Voltage-sensitive dyes reveal a modular organization in monkey striate cortex. Nature 321, 579–85. https://doi.org/10.1038/321579a0

Bosking, W.H., Zhang, Y., Schofield, B., Fitzpatrick, D., 1997. Orientation selectivity and the arrangement of horizontal connections in tree shrew striate cortex. J Neurosci 17, 2112–27.

Cardin, J.A., Crair, M.C., Higley, M.J., 2020. Mesoscopic Imaging: Shining a Wide Light on Large-Scale Neural Dynamics. Neuron 108, 33–43. https://doi.org/10.1016/j.neuron.2020.09.031

Carrillo-Reid, L., Yang, W., Kang Miller, J., Peterka, D.S., Yuste, R., 2017. Imaging and Optically Manipulating Neuronal Ensembles. Annu. Rev. Biophys. 46, 271–293. https://doi.org/10.1146/annurev-biophys-070816-033647

Chapman, B., Stryker, M.P., Bonhoeffer, T., 1996. Development of orientation preference maps in ferret primary visual cortex. J Neurosci 16, 6443–53.
Chen, T.W., Wardill, T.J., Sun, Y., Pulver, S.R., Renninger, S.L., Baohan, A., Schreiter, E.R., Kerr, R.A., Orger, M.B., Jayaraman, V., Looger, L.L., Svoboda, K., Kim, D.S., 2013. Ultrasensitive fluorescent proteins for imaging neuronal activity. Nature 499, 295–300. https://doi.org/10.1038/nature12354
Chuong, A.S., Miri, M.L., Busskamp, V., Matthews, G.A.C., Acker, L.C., Sørensen, A.T., Young, A., Klapoetke, N.C., Henninger, M.A., Kodandaramaiah, S.B., Ogawa, M., Ramanlal, S.B., Bandler, R.C., Allen, B.D., Forest, C.R., Chow, B.Y., Han, X., Lin, Y., Tye, K.M., Roska, B., Cardin, J.A., Boyden, E.S., 2014. Noninvasive optical inhibition with a red-shifted microbial rhodopsin. Nat. Neurosci. 17, 1123–1129. https://doi.org/10.1038/nn.3752
Deisseroth, K., 2015. Optogenetics: 10 years of microbial opsins in neuroscience. Nat. Neurosci. 18, 1213–1225. https://doi.org/10.1038/nn.4091
Edelstein, A., Amodaj, N., Hoover, K., Vale, R., Stuurman, N., 2010. Computer control of microscopes using microManager. Curr Protoc Mol Biol Chapter 14, Unit14 20. https://doi.org/10.1002/0471142727.mb1420s92
Ghanbari, L., Carter, R.E., Rynes, M.L., Dominguez, J., Chen, G., Naik, A., Hu, J., Sagar, M.A.K., Haltom, L., Mossazghi, N., 2019. Cortex-wide neural interfacing via transparent polymer skulls. Nat. Commun. 10, 1–13.
Gilbert, C.D., Wiesel, T.N., 1989. Columnar specificity of intrinsic horizontal and corticocortical connections in cat visual cortex. J Neurosci 9, 2432–42.
Gradinaru, V., Zhang, F., Ramakrishnan, C., Mattis, J., Prakash, R., Diester, I., Goshen, I., Thompson, K.R., Deisseroth, K., 2010. Molecular and Cellular Approaches for Diversifying and Extending Optogenetics. Cell 141, 154–165. https://doi.org/10.1016/j.cell.2010.02.037
Grinvald, A., Hildesheim, R., 2004. VSDI: a new era in functional imaging of cortical dynamics. Nat. Rev. Neurosci. 5, 874–885. https://doi.org/10.1038/nrn1536
Grinvald, A., Lieke, E., Frostig, R.D., Gilbert, C.D., Wiesel, T.N., 1986. Functional architecture of cortex revealed by optical imaging of intrinsic signals. Nature 324, 361–364. https://doi.org/10.1038/324361a0
Hubel, D.H., Wiesel, T.N., 1997. Ferrier lecture - Functional architecture of macaque monkey visual cortex. Proc. R. Soc. Lond. B Biol. Sci. 198, 1–59. https://doi.org/10.1098/rspb.1977.0085
Hubel, D.H., Wiesel, T.N., 1968. Receptive fields and functional architecture of monkey striate cortex. J Physiol 195, 215–43.
Issa, N.P., Trepel, C., Stryker, M.P., 2000. Spatial frequency maps in cat visual cortex. J Neurosci 20, 8504–14.
Kaas, J.H., Nelson, R.J., Sur, M., Lin, C.-S., Merzenich, M.M., 1979. Multiple Representations of the Body Within the Primary Somatosensory Cortex of Primates. Science 204, 521–523.
Kara, P., Boyd, J.D., 2009. A micro-architecture for binocular disparity and ocular dominance in visual cortex. Nature 458, 627–31. https://doi.org/10.1038/nature07721
Kaschube, M., Schnabel, M., Lowel, S., Coppola, D.M., White, L.E., Wolf, F., 2010. Universality in the evolution of orientation columns in the visual cortex. Science 330, 1113–6. https://doi.org/10.1126/science.1194869
Kenet, T., Bibitchkov, D., Tsodyks, M., Grinvald, A., Arieli, A., 2003. Spontaneously emerging cortical representations of visual attributes. Nature 425, 954–6. https://doi.org/10.1038/nature02078
Klapoetke, N.C., Murata, Y., Kim, S.S., Pulver, S.R., Birdsey-Benson, A., Cho, Y.K., Morimoto, T.K., Chuong, A.S., Carpenter, E.J., Tian, Z., Wang, J., Xie, Y., Yan, Z., Zhang, Y., Chow, B.Y., Surek, B., Melkonian, M., Jayaraman, V., Constantine-Paton, M., Wong,

G.K., Boyden, E.S., 2014. Independent optical excitation of distinct neural populations. Nat Methods 11, 338–46. https://doi.org/10.1038/nmeth.2836

Malach, R., Amir, Y., Harel, M., Grinvald, A., 1993. Relationship between intrinsic connections and functional architecture revealed by optical imaging and in vivo targeted biocytin injections in primate striate cortex. Proc Natl Acad Sci U A 90, 10469–73.

Merzenich, M.M., Knight, P.L., Roth, G.L., 1975. Representation of cochlea within primary auditory cortex in the cat. J. Neurophysiol. 38, 231–249. https://doi.org/10.1152/jn.1975.38.2.231

Mulholland, H.N., Hein, B., Kaschube, M., Smith, G.B., 2021. Tightly coupled inhibitory and excitatory functional networks in the developing primary visual cortex. eLife 10, e72456. https://doi.org/10.7554/eLife.72456

Musall, S., Kaufman, M.T., Juavinett, A.L., Gluf, S., Churchland, A.K., 2019. Single-trial neural dynamics are dominated by richly varied movements. Nat. Neurosci. 22, 1677–1686. https://doi.org/10.1038/s41593-019-0502-4

Packer, A.M., Roska, B., Häusser, M., 2013. Targeting neurons and photons for optogenetics. Nat. Neurosci. 16, 805–815. https://doi.org/10.1038/nn.3427

Peirce, J.W., 2007. PsychoPy--Psychophysics software in Python. J Neurosci Methods 162, 8–13. https://doi.org/10.1016/j.jneumeth.2006.11.017

Ratzlaff, E.H., Grinvald, A., 1991. A tandem-lens epifluorescence macroscope: Hundred-fold brightness advantage for wide-field imaging. J. Neurosci. Methods 36, 127–137. https://doi.org/10.1016/0165-0270(91)90038-2

Ren, C., Komiyama, T., 2021. Characterizing Cortex-Wide Dynamics with Wide-Field Calcium Imaging. J. Neurosci. 41, 4160–4168. https://doi.org/10.1523/JNEUROSCI.3003-20.2021

Roy, A., Osik, J.J., Ritter, N.J., Wang, S., Shaw, J.T., Fiser, J., Van Hooser, S.D., 2016. Optogenetic spatial and temporal control of cortical circuits on a columnar scale. J Neurophysiol 115, 1043–62. https://doi.org/10.1152/jn.00960.2015

Smith, G.B., Fitzpatrick, D., 2016. Viral Injection and Cranial Window Implantation for In Vivo Two-Photon Imaging. Methods Mol Biol 1474, 171–85. https://doi.org/10.1007/978-1-4939-6352-2_10

Smith, G.B., Hein, B., Whitney, D.E., Fitzpatrick, D., Kaschube, M., 2018. Distributed network interactions and their emergence in developing neocortex. Nat. Neurosci. 21, 1600–1608. https://doi.org/10.1038/s41593-018-0247-5

Smith, G.B., Whitney, D.E., Fitzpatrick, D., 2015. Modular Representation of Luminance Polarity in the Superficial Layers of Primary Visual Cortex. Neuron 88, 805–18. https://doi.org/10.1016/j.neuron.2015.10.019

Tremblay, S., Acker, L., Afraz, A., Albaugh, D.L., Amita, H., Andrei, A.R., Angelucci, A., Aschner, A., Balan, P.F., Basso, M.A., Benvenuti, G., Bohlen, M.O., Caiola, M.J., Calcedo, R., Cavanaugh, J., Chen, Y., Chen, S., Chernov, M.M., Clark, A.M., Dai, J., Debes, S.R., Deisseroth, K., Desimone, R., Dragoi, V., Egger, S.W., Eldridge, M.A.G., El-Nahal, H.G., Fabbrini, F., Federer, F., Fetsch, C.R., Fortuna, M.G., Friedman, R.M., Fujii, N., Gail, A., Galvan, A., Ghosh, S., Gieselmann, M.A., Gulli, R.A., Hikosaka, O., Hosseini, E.A., Hu, X., Hüer, J., Inoue, K., Janz, R., Jazayeri, M., Jiang, R., Ju, N., Kar, K., Klein, C., Kohn, A., Komatsu, M., Maeda, K., Martinez-Trujillo, J.C., Matsumoto, M., Maunsell, J.H.R., Mendoza-Halliday, D., Monosov, I.E., Muers, R.S., Nurminen, L., Ortiz-Rios, M., O'Shea, D.J., Palfi, S., Petkov, C.I., Pojoga, S., Rajalingham, R., Ramakrishnan, C., Remington, E.D., Revsine, C., Roe, A.W., Sabes, P.N., Saunders, R.C., Scherberger, H., Schmid, M.C., Schultz, W., Seidemann, E., Senova, Y.-S., Shadlen, M.N., Sheinberg, D.L., Siu, C., Smith, Y., Solomon, S.S., Sommer, M.A., Spudich, J.L., Stauffer, W.R., Takada, M., Tang, S., Thiele, A., Treue, S., Vanduffel, W., Vogels, R., Whitmire, M.P., Wichmann, T., Wurtz, R.H., Xu, H., Yazdan-Shahmorad, A.,

Shenoy, K.V., DiCarlo, J.J., Platt, M.L., 2020. An Open Resource for Non-human Primate Optogenetics. Neuron 108, 1075-1090.e6. https://doi.org/10.1016/j.neuron.2020.09.027

Virtanen, P., Gommers, R., Oliphant, T.E., Haberland, M., Reddy, T., Cournapeau, D., Burovski, E., Peterson, P., Weckesser, W., Bright, J., van der Walt, S.J., Brett, M., Wilson, J., Millman, K.J., Mayorov, N., Nelson, A.R.J., Jones, E., Kern, R., Larson, E., Carey, C.J., Polat, İ., Feng, Y., Moore, E.W., VanderPlas, J., Laxalde, D., Perktold, J., Cimrman, R., Henriksen, I., Quintero, E.A., Harris, C.R., Archibald, A.M., Ribeiro, A.H., Pedregosa, F., van Mulbregt, P., SciPy 1.0 Contributors, 2020. SciPy 1.0: Fundamental Algorithms for Scientific Computing in Python. Nat. Methods 17, 261–272. https://doi.org/10.1038/s41592-019-0686-2

Weliky, M., Bosking, W.H., Fitzpatrick, D., 1996. A systematic map of direction preference in primary visual cortex. Nature 379, 725–8. https://doi.org/10.1038/379725a0

West, S.L., Aronson, J.D., Popa, L.S., Feller, K.D., Carter, R.E., Chiesl, W.M., Gerhart, M.L., Shekhar, A.C., Ghanbari, L., Kodandaramaiah, S.B., Ebner, T.J., 2022. Wide-Field Calcium Imaging of Dynamic Cortical Networks during Locomotion. Cereb. Cortex N. Y. N 1991 32, 2668–2687. https://doi.org/10.1093/cercor/bhab373

Wilson, D.E., Scholl, B., Fitzpatrick, D., 2018. Differential tuning of excitation and inhibition shapes direction selectivity in ferret visual cortex. Nature 560, 97–101. https://doi.org/10.1038/s41586-018-0354-1

Zhang, Y., Rózsa, M., Liang, Y., Bushey, D., Wei, Z., Zheng, J., Reep, D., Broussard, G.J., Tsang, A., Tsegaye, G., Narayan, S., Obara, C.J., Lim, J.-X., Patel, R., Zhang, R., Ahrens, M.B., Turner, G.C., Wang, S.S.-H., Korff, W.L., Schreiter, E.R., Svoboda, K., Hasseman, J.P., Kolb, I., Looger, L.L., 2023. Fast and sensitive GCaMP calcium indicators for imaging neural populations. Nature 615, 884–891. https://doi.org/10.1038/s41586-023-05828-9

Figure legends

Figure 1. Optical design of opto-macroscope. a. Schematic of light path. 590 nm laser output (orange line) is directed through a power-control AOM, with the 1st-order diffracted beam coupled into a Polygon DMD module. Patterned stimulation light is directed onto the sample with a short-pass dichroic. GCaMP excitation light (blue line) enters the opto-macroscope below the stimulation path and is directed onto the sample with a long-pass dichroic. GCaMP emission (green line) reaches the sCMOS camera passing through both the imaging and stimulation dichroic mirrors. Stray stimulation light is blocked from reaching the camera with a combination of bandpass, shortpass and notch filters. Some stray stimulation light is collected onto a photodiode to provide high accuracy timing measurements. Full details provided in methods. **b**. Opto-macroscope as built. **c**. Filter design for simultaneous imaging and stimulation, showing excitation and emission spectra for GCaMP. Key filters and dichroic mirrors are indicated.

Figure 2: Optical properties of the opto-macroscope. a. The system can readily generate spatially complex arbitrary patterns over a large area. Left column shows requested input pattern, right shows projected pattern at the sample plane. The addressable stimulation area is ~3.8 mm diameter. **b-c.** Spatial resolution of imaging (**b**) and stimulation (**c**) paths using USAF 1951 targets. Top images show full FOV, bottom is zoomed in view of area in red box above. Imaging resolution is greater than 143.7 lp/mm, and stimulation resolution is greater than 40.3 lp/mm. **d.** Stimulation resolution assayed by projecting a single pixel grid on a camera placed at the sample plane is 8.0 μm FWHM. Black line: measured points, gray shading: mean±SEM across grid lines, red line: gaussian fit. **e.** *Left:* X-Z projection obtained by imaging a 15 μm bead. FWHM in axial dimension is 151 μm. *Right:* X-Z projection obtained by projecting a 40 x 40 μm square on a camera translated about the focal plane. FWHM is 594 μm. **f**. Horizontal line profiles taken at axial positions indicated in (e) for imaging (*Top*) and stimulation (*bottom*). **g**. Uniformity of stimulation power density across the addressable area, measured with 125 x 125 μm squares. **h**. Stimulation uniformity measured by projecting full-area stimulation on camera mounted at focal plane. *Left*: camera image of stimulation illumination. *Right*: Line profiles taken at locations shown. **i.** Absence of stimulation light artifacts in GCaMP imaging with optogenetic stimulation. *Left*: Experimental schematic of imaging in animal expressing only GCaMP (no Chrimson). *Left trace:* Spontaneous neural activity, zoomed in on two example events (average ΔF across FOV). *Right trace:* GCaMP fluorescence (during a period without spontaneous activity) in presence of increasing stimulation power. Black trace shows stimulus triggered average (+/- SEM) response across repeated train of optogenetic stimulations (9 power increments, n=10 trials). Y axis scale matched to spontaneous trace on left. Green trace shows zoomed in view. Blue trace shows fluorescence of a static fluorescein sample. Time 0 on x-axis indicates onset of first optogenetic stimulation (black and green trace), or beginning of acquisition (blue trace). **j**. Stability of stimulation laser power over tens of minutes (*Top*) or seconds (*Bottom*).

Figure 3: Fast and specific temporal modulation of opto-stimulation power. a-c. AOM control of output laser intensity allows for complex temporal modulation of stimulus power, accurately producing increasing and decreasing linear ramps (**a**), changes in temporal frequency of pulse trains (**b**), and high frequency stimulation (**c**) (1 ms pulse, 500hz). (*Top*) User specified laser power waveform. (*Bottom*) Power measured at imaging focus plane using a high speed photodiode. **d-f**. Independent power control for individual stimulation patterns. **d.** (*Left*) Stimulus pattern inputs. (*Right*) Camera images of stimulated patterns projected onto a

fluorescent slide. ROIs of a single stimulated region outline in color coded dashed lines. **e.** Stimulating both patterns at the same stimulus power. (*Top*) Opto-stimulus power density (7.58 mW/mm^2) with laser ON periods indicated in red. ID of specific pattern being delivered at a given time is indicated above. (*Bottom*) Measured fluorescent counts (normalized to maximum) from imaging camera within each pattern's ROI over trial duration. **f.** Same as **e**, but now stimulating pattern 2 at half the power (3.78 mW/mm^2) of pattern 1.

Figure 4: Simultaneous mesoscopic calcium imaging and optogenetic stimulation in ferret visual cortex. a. Experimental schematic. AAVs expressing GCaMP6s and ChrimsonR-ST-mRuby are co-injected into young ferret visual cortex and then imaged with the opto-macroscope. **b**. Coronal sections of fixed tissue showing expression of GCaMP and ChrimsonR ferret visual cortex. **c**. Zoomed-in image showing localization of somatically-targeted (ST) ChrimsonR predominantly to soma and proximal neurites. **d**. Functional imaging of optogenetic stimulation targeted to four separate stimulus ROIs. ROIs stimulated one at a time, in sequence (1 second stimulus duration, 4 second ISI). **e**. Opto-stimulation drives strong and reliable columnar responses. (*Left*) Opto-stimulus ROIs, overlaid onto imaging GCaMP FOV. (*Middle*) Stimulus triggered average response of pixels within each stimulus ROI (mean, +/- SEM) (n trials=20 per stimulus). (*Right*) Average response across imaging FOV. **f**. Raster of average ΔF/F within each stimulus ROI during full trial duration, sorted by stimulus ID. Optogenetic stimulation drove spatially specific activity within its respective ROI, with limited cross activation. Periods of ROI stimulus onset and offset indicated with color coded dashed lines. **g**. Average ΔF/F response as a function of pixel distance from stimulation ROI center, showing that optogenetic stimulation robustly drives activity locally (error bars show mean +/- std. dev across pixels within distance bin). **h**. Average ΔF/F within stimulus ROI as a function of increasing stimulus size for animals expressing GCaMP6s and ChrimsonR (red) or GCaMP6s alone (gray).

Figure 5: Optogenetic stimulation of functionally relevant cortical network patterns. a. Visually evoked responses to ON or OFF full screen luminance changes. (*Middle*) Stimulus triggered average response across FOV (n trials=40, grey=individual trials, black=mean (+/- SEM)). (*Right*) Average ON and OFF evoked patterns. **b.** ON/OFF luminance preference map. Online analysis of OFF preferring regions outlined in black. **c.** Opto-stimulation ROIs based on OFF pattern, drawn from online analysis of visually evoked responses during experiment. **d.** Time series calcium response to opto-stimulation of OFF pattern (single trial example). **e.** Stimulus triggered average response of pixels located within (orange) or outside of (blue) the stimulus ROI show reliable evoked calcium activity (n trials=20, mean +/- SEM). **f.** Average opto-evoked response. (*Left)* Mean of raw ΔF/F activity. (*Right*) Mean of spatially filtered activity. **g.** Spontaneous activity in developing ferret visual cortex. (*Left)* Mean response across FOV, showing multiple spontaneous events. (*Right)* Two example events, spatially filtered. **h.** Spontaneous correlation map calculated from all detected events. Online analysis of regions that were positively correlated with the seed point (green dot) outlined in black. **i.** Opto-stimulation ROI based on spontaneous correlation pattern. **j- l.** Same as **d-f**, but for stimulus based on spontaneous correlation pattern.

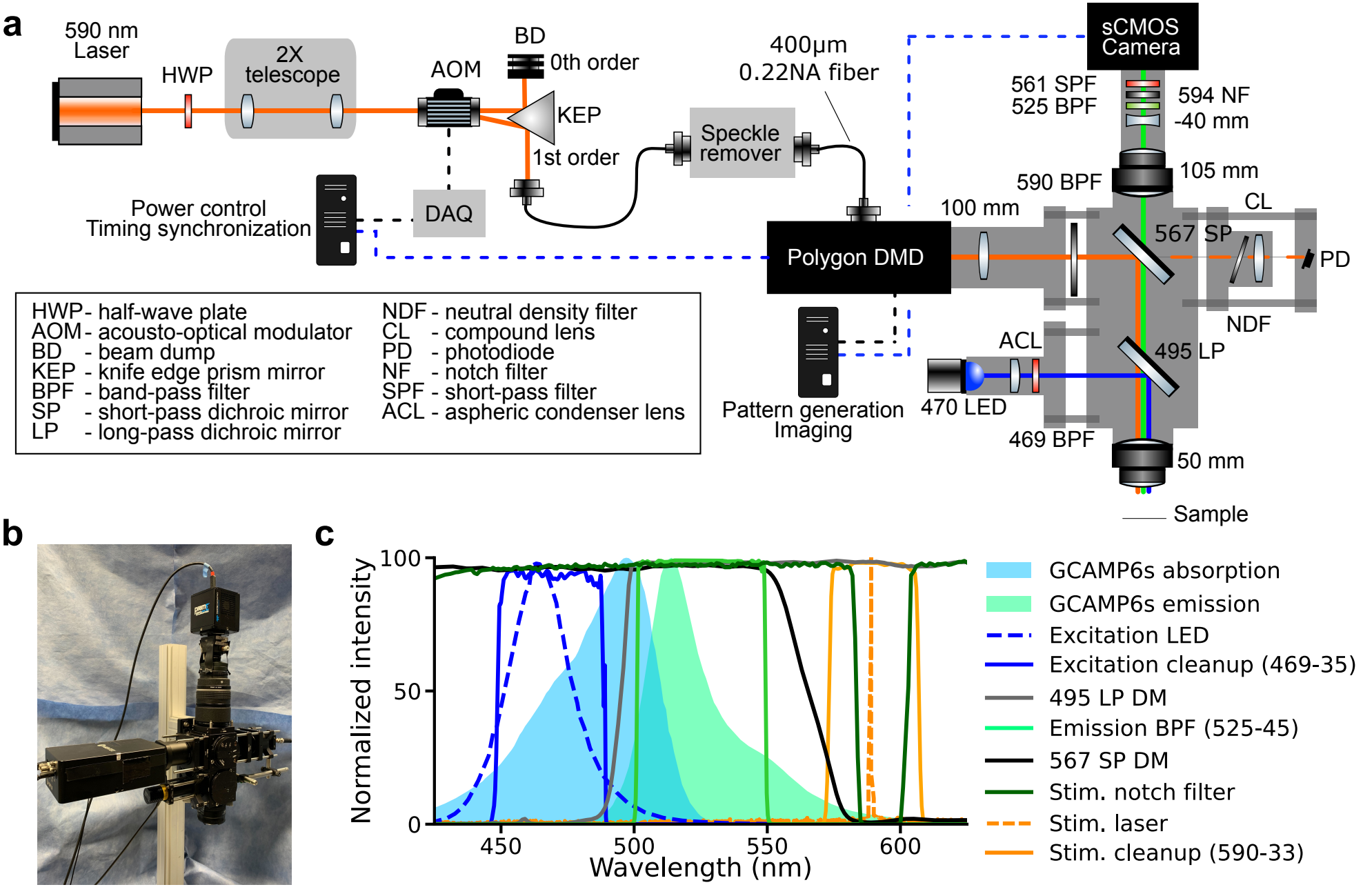
a
590 nm Laser
HWP
2X telescope
AOM
BD
0th order
KEP
1st order
400µm 0.22NA fiber
Speckle remover
sCMOS Camera
561 SPF
525 BPF
594 NF
-40 mm
105 mm
590 BPF
CL
100 mm
567 SP
PD
NDF
Power control
Timing synchronization
DAQ
Polygon DMD
ACL
495 LP
470 LED
469 BPF
50 mm
Pattern generation
Imaging
Sample
HWP - half-wave plate
AOM - acousto-optical modulator
BD - beam dump
KEP - knife edge prism mirror
BPF - band-pass filter
SP - short-pass dichroic mirror
LP - long-pass dichroic mirror
NDF - neutral density filter
CL - compound lens
PD - photodiode
NF - notch filter
SPF - short-pass filter
ACL - aspheric condenser lens
b
c
Normalized intensity
100
50
0
450
500
550
600
Wavelength (nm)
GCAMP6s absorption
GCAMP6s emission
Excitation LED
Excitation cleanup (469-35)
495 LP DM
Emission BPF (525-45)
567 SP DM
Stim. notch filter
Stim. laser
Stim. cleanup (590-33)

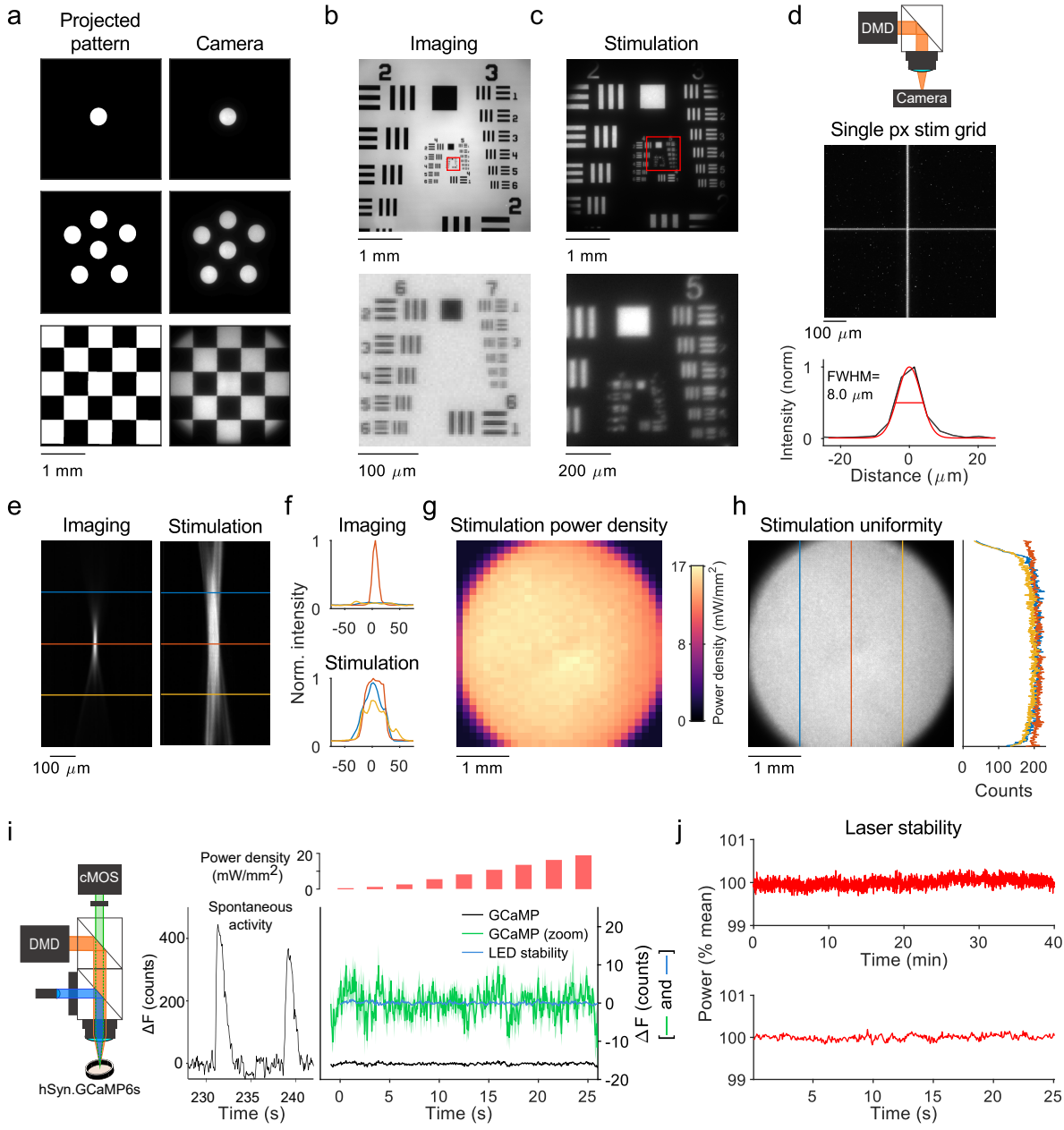
a
Projected pattern
Camera
1 mm
b
Imaging
1 mm
100 μm
c
Stimulation
1 mm
200 μm
d
DMD
Camera
Single px stim grid
100 μm
Intensity (norm)
FWHM= 8.0 μm
Distance (μm)
e
Imaging
Stimulation
100 μm
f
Imaging
Stimulation
Norm. intensity
g
Stimulation power density
Power density (mW/mm2)
1 mm
h
Stimulation uniformity
1 mm
Counts
i
cMOS
DMD
hSyn.GCaMP6s
Power density (mW/mm2)
Spontaneous activity
ΔF (counts)
Time (s)
GCaMP
GCaMP (zoom)
LED stability
ΔF (counts) [— and —]
j
Laser stability
Power (% mean)
Time (min)
Time (s)

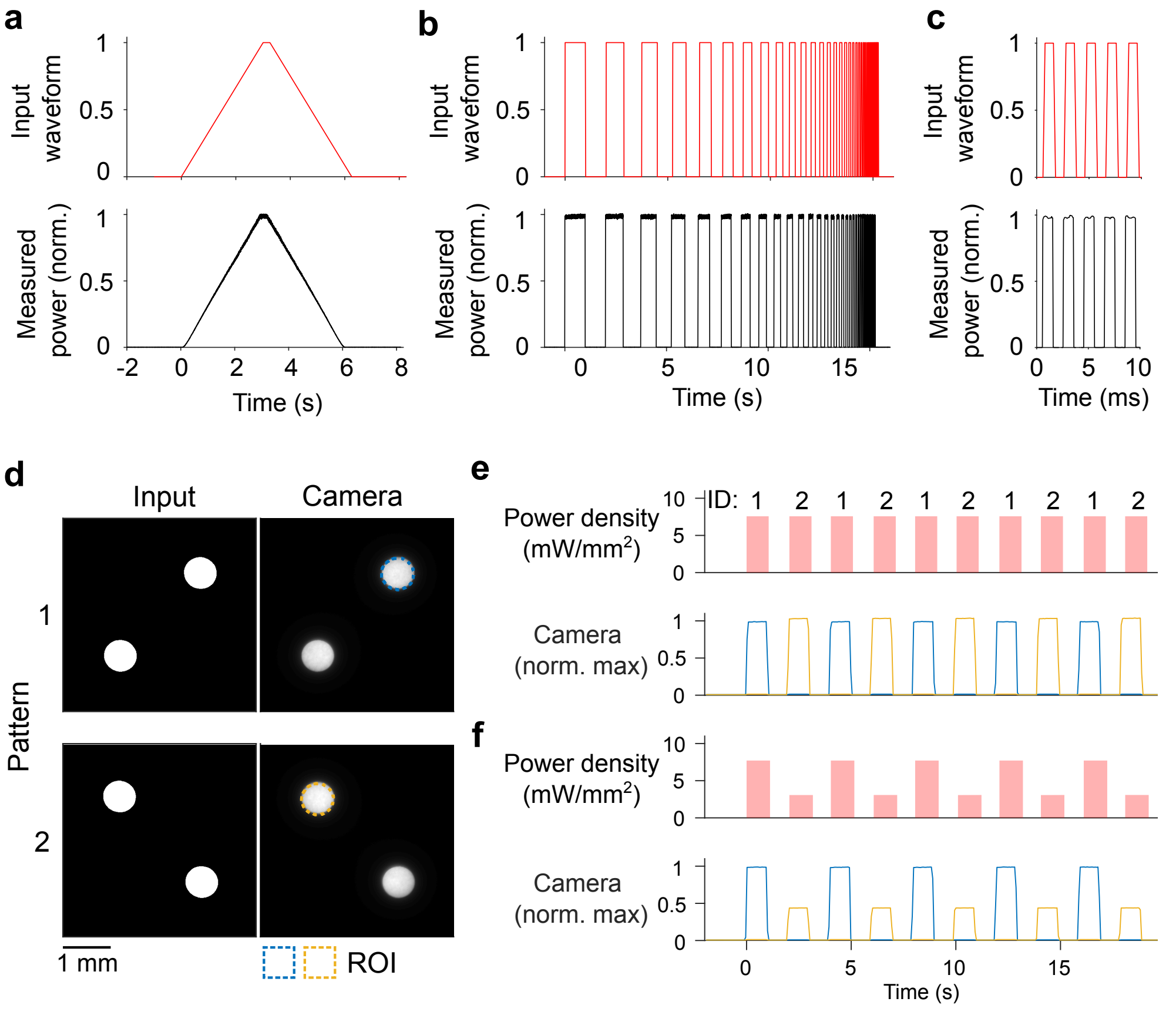
a
b
c
Input waveform
Measured power (norm.)
1
0.5
0
-2
0
2
4
6
8
Time (s)
0
5
10
15
Time (s)
0
5
10
Time (ms)
d
Input
Camera
Pattern
1
2
1 mm
ROI
e
Power density (mW/mm²)
ID: 1 2 1 2 1 2 1 2 1 2
10
5
0
Camera (norm. max)
1
0.5
f
Time (s)

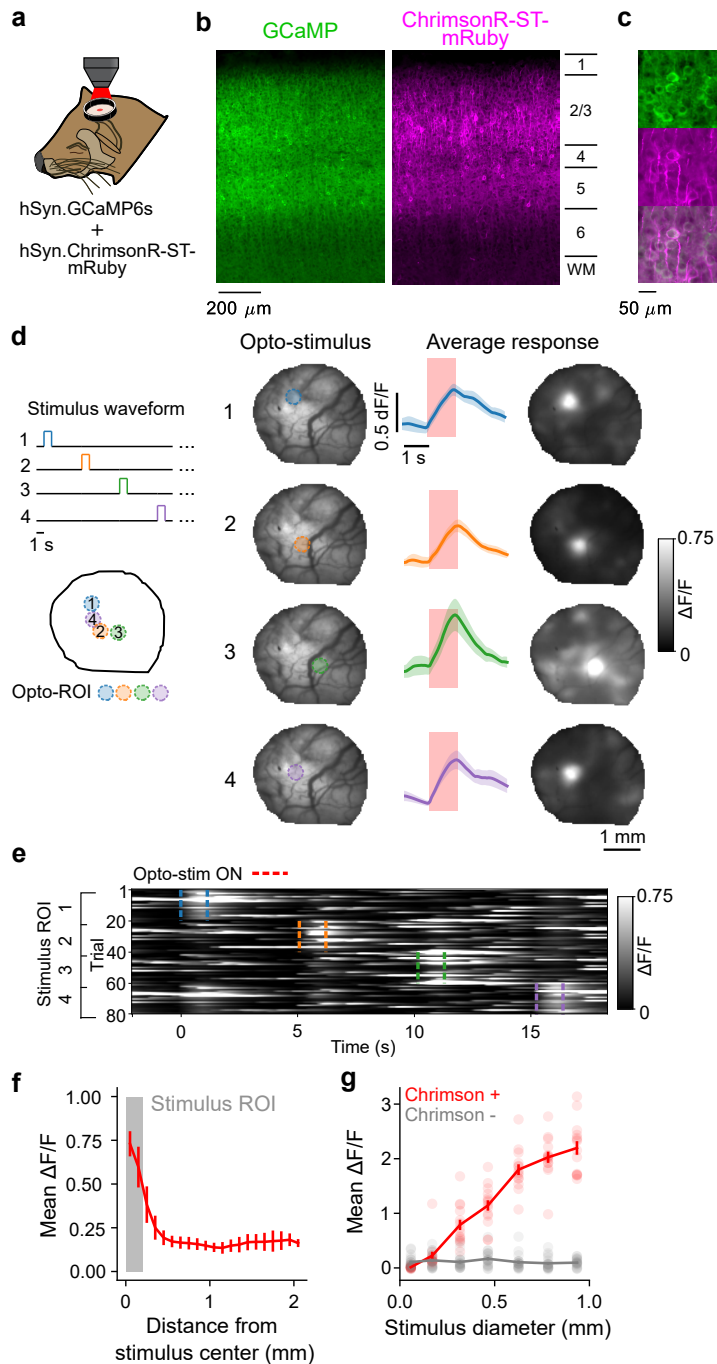
a
hSyn.GCaMP6s
+
hSyn.ChrimsonR-ST-mRuby
b
GCaMP
ChrimsonR-ST-mRuby
1
2/3
4
5
6
WM
200 μm
c
50 μm
d
Opto-stimulus
Average response
Stimulus waveform
1
2
3
4
1 s
Opto-ROI
0.5 dF/F
1 s
0.75
ΔF/F
0
1 mm
e
Opto-stim ON
Stimulus ROI
Trial
Time (s)
f
Stimulus ROI
Mean ΔF/F
Distance from stimulus center (mm)
g
Chrimson +
Chrimson -
Mean ΔF/F
Stimulus diameter (mm)

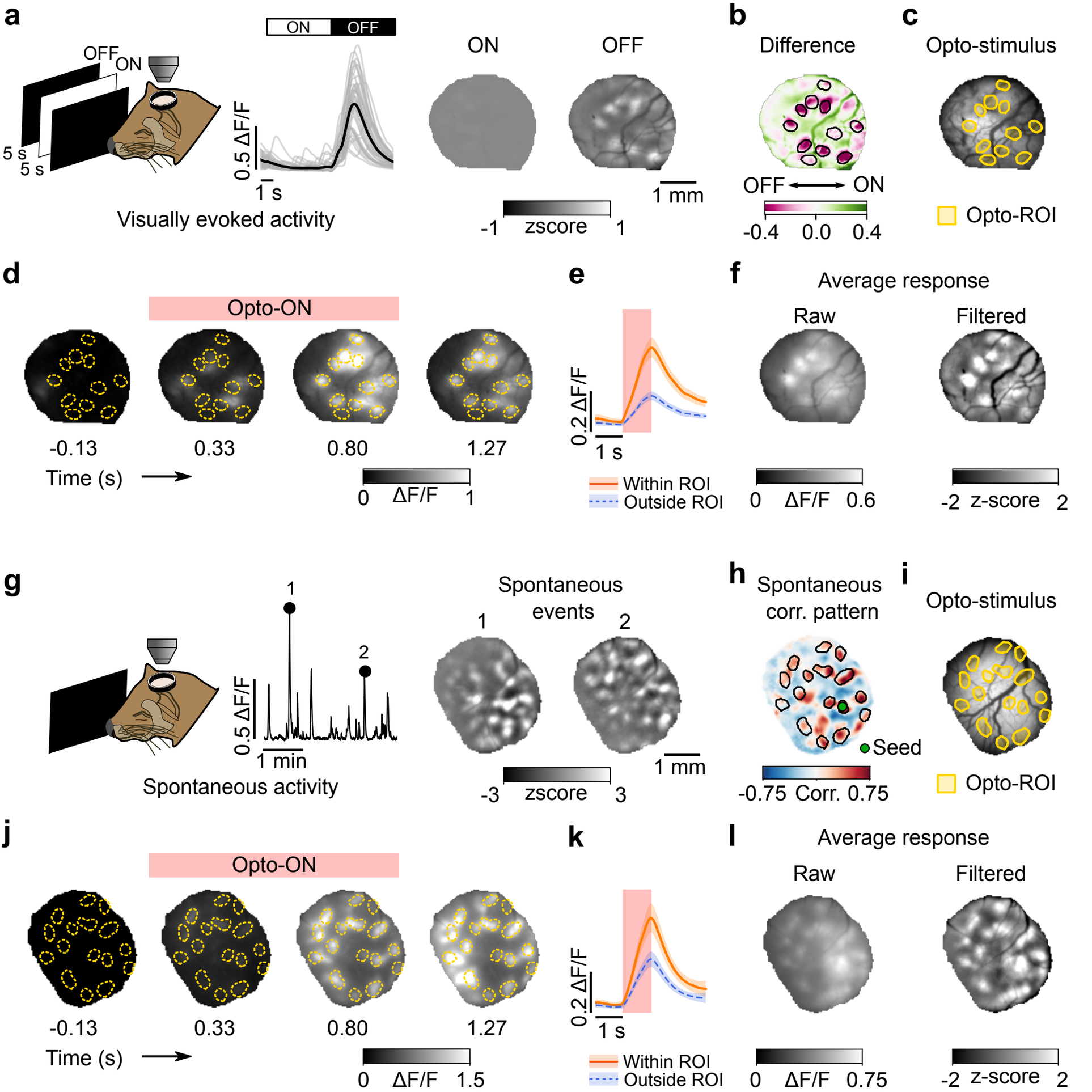
a
ON
OFF
OFF
ON
5 s
5 s
0.5 ΔF/F
1 s
Visually evoked activity
ON
OFF
1 mm
-1
zscore
1
b
Difference
OFF
ON
-0.4
0.0
0.4
c
Opto-stimulus
Opto-ROI
d
Opto-ON
-0.13
0.33
0.80
1.27
Time (s)
0
ΔF/F
1
e
0.2 ΔF/F
1 s
Within ROI
Outside ROI
f
Average response
Raw
Filtered
0
ΔF/F
0.6
-2
z-score
2
g
1
2
0.5 ΔF/F
1 min
Spontaneous activity
Spontaneous events
1
2
1 mm
-3
zscore
3
h
Spontaneous corr. pattern
Seed
-0.75
Corr.
0.75
i
Opto-stimulus
Opto-ROI
j
Opto-ON
-0.13
0.33
0.80
1.27
Time (s)
0
ΔF/F
1.5
k
0.2 ΔF/F
1 s
Within ROI
Outside ROI
l
Average response
Raw
Filtered
0
ΔF/F
0.75
-2
z-score
2